

Turbulence production by nonbreaking waves: Laboratory and numerical simulations

Ivan B. Savelyev,¹ Eric Maxeiner,² and Dmitry Chalikov^{3,4}

Received 28 January 2012; revised 10 April 2012; accepted 26 April 2012; published 7 June 2012.

[1] This paper investigates the effect of wave motion on the turbulence in close proximity to the surface. Some existing theories suggest mechanisms by which the energy is transferred from waves to turbulence. However, scarce empirical results struggle to establish the existence of such energy transfer and are not sufficient for thorough validation of existing theories. The present investigation relies on both experimental and numerical approaches. Turbulent velocities at the water surface were measured in a laboratory wave tank with high precision using the thermal-marking velocimetry technique. Numerically, a fully nonlinear model for the wave motion was coupled with Large Eddy Simulation for the turbulent motion. The results confirm the turbulence production due to wave motion. The turbulent kinetic energy was found to be a function of time, wave steepness, wave phase, and initial turbulent conditions. Additionally, turbulent motion near the surface was found to be horizontally anisotropic due to the formation of near-surface eddies, elongated in the direction of wave propagation.

Citation: Savelyev, I. B., E. Maxeiner, and D. Chalikov (2012), Turbulence production by nonbreaking waves: Laboratory and numerical simulations, *J. Geophys. Res.*, 117, C00J13, doi:10.1029/2012JC007928.

1. Introduction

[2] Historically the parameterization of turbulence production in the upper ocean has primarily relied on the assumptions of wall turbulence, where the wind-generated surface friction velocity acts as a moving boundary. In more complete parameterizations an additional term is added in the top few meters to account for the dissipation of breaking surface waves (see detailed overview in *Drennan et al.* [1997]). These two mechanisms are indeed responsible for the bulk of the produced turbulence and rightfully deserve the attention of the large number of papers written on the subject. However, there exists a distinct third mechanism, first described by *Phillips* [1961], in which turbulence is produced due to wave-turbulence interaction. Its contribution has been considered relatively small and is therefore typically neglected in practical applications. However, recent evidence suggests that in some scenarios dissipation due to wave-turbulence interaction is not negligible. For example, *Ardhuin and Jenkins* [2006] demonstrated its importance in attenuation of swell propagating across the Pacific Ocean.

In a laboratory experiment, *Milgram* [1998] studied the dissipation of capillary waves due to preexisting background turbulence, motivated by remote sensing applications that are sensitive to the slope distribution of very young waves. Finally, Stokes drift associated with the wave motion interacts with the turbulence produced near the surface, stretches vorticity horizontally, and forms a field of elongated eddies, known as Langmuir circulations [*Craik and Leibovich*, 1976]. These circulations are now believed to affect the depth of the mixed layer and to be one of the primary mechanisms for vertical transport in the upper ocean [*Thorpe*, 2004].

[3] Currently there are a number of competing theories and hypotheses attempting to explain the mechanism of wave-induced turbulence production. The variety of approaches is caused, perhaps, both by the complexity of the problem and by the lack of detailed experimental data. *Babanin* [2006] hypothesized that a monochromatic wave in an otherwise quiescent fluid will produce turbulence if a critical wave Reynolds number, Re_w , is exceeded. This parameter is defined as $Re_w = a^2 \omega / \nu$, where a is the wave amplitude, ω is radial wave frequency, and ν is kinematic viscosity. In a later laboratory experiment, *Babanin and Haus* [2009] detected signs of Kolmogorov turbulent spectra, signifying the presence of turbulence produced by such waves. In another laboratory experiment, *Dai et al.* [2010] estimated the critical wave Reynolds number indirectly by measuring the rate of destratification of initial vertical temperature profile and found qualitative agreement with *Babanin* [2006].

[4] After some analysis of governing equations, authors of most theoretical papers on the subject [e.g., *McWilliams et al.*, 1997; *Drennan et al.*, 1997; *Teixeira and Belcher*, 2002] arrived at the conclusion that the turbulence is

¹Naval Research Laboratory, Washington, D. C., USA.

²National Research Council, Naval Research Laboratory, Washington, D. C., USA.

³Faculty of Engineering and Industrial Sciences, Swinburne University of Technology, Melbourne, Victoria, Australia.

⁴St. Petersburg Branch, P. P. Shirshov Institute of Oceanology, RAS, Saint Petersburg, Russia.

Corresponding author: I. B. Savelyev, Naval Research Laboratory, Code 7233, 4555 Overlook Ave. SW, Washington, DC 20375, USA. (ivan.savelyev@nrl.navy.mil)

produced by the interaction of a nonzero Reynolds stress and a vertical profile of horizontal velocity, more specifically the Stokes drift:

$$P = \rho_w \overline{u_x u_z} \frac{\partial U_x}{\partial z}, \quad (1)$$

where P is turbulence production, ρ_w is the water density, u_x and u_z are horizontal and vertical turbulent velocities, and U_x is Stokes drift velocity. The nonzero value of Reynolds stress $\overline{u_x u_z}$ is generally expected to be entirely due to the turbulent motion. However, *Cheung and Street* [1988] in their laboratory experiment observed some signs of rotationality in the flow field of the wave, leading to a contribution from wave orbital velocities to the Reynolds stress. More recently, *Yuan et al.* [2010] obtained a unified wave theory without the assumption of irrotationality. The theory also suggests a nonzero vertical flux due to the linear wave motion.

[5] In practice, a more important problem is the interaction of waves with preexisting turbulence rather than the origination of wave-induced turbulence, because the upper ocean tends to always be in motion due to the presence of other sources of turbulence. Moreover, since the production of turbulence is a function of preexisting turbulence (see equation (1)), in theoretical and numerical models it is meaningful to assume certain initial turbulent conditions and investigate their growth or decay in time. Such approach was taken within the numerical investigations by *Teixeira and Belcher* [2002, 2010], as well as within the numerical investigations presented in this paper. Qualitatively both models agree that the initial turbulent kinetic energy grows due to the wave-turbulence interaction. However, there are significant differences in the wave phase dependence and in the directionality of turbulent properties that are discussed in greater detail below.

[6] Experimental data on wave-induced turbulence production are very limited. Moreover, most of the papers that are available on the subject basically acknowledge the existence of such process, but are unable to quantify its properties thoroughly due to large statistical uncertainties. The difficulties arise due to the slow motion of the wave-induced turbulence compared to the surrounding wave orbital motion. In addition, the measurements must be made near the moving boundary, preferably near sharp wave crests where the shear flow due to Stokes drift is greatest. Studies using laboratory experiments include *Cheung and Street* [1988], *Milgram* [1998], *Babanin and Haus* [2009] and *Dai et al.* [2010]. In field studies, additional challenges come from the simultaneous existence of other turbulence production mechanisms, as well as from the orbital motion of waves of various scales, including the same scales as the turbulent motion. To our knowledge the only successful direct measurements in the field were conducted by *Veron et al.* [2008, 2009], which found an increase in wave-coherent turbulence intensity with wave steepness. Also, *Huang and Qiao* [2010] analyzed field data with the help of a 1-D turbulence closure scheme and came to the conclusion that waves attenuate proportionally to square root of wave steepness due to the wave turbulence energy flux.

[7] The experimental studies listed above primarily focus on the existence of turbulent kinetic energy (TKE),

$$\langle q^2 \rangle = \langle u_x^2 + u_y^2 + u_z^2 \rangle, \quad (2)$$

and its dependence on wave parameters. However, little attention was paid to directionality and wave phase dependence of these turbulent motions. An exception to this are the numerical predictions of *Teixeira and Belcher* [2002] which describe a mechanism by which the vorticity is stretched by wave crests and troughs, consequently causing the formation of horizontally elongated vortices. Together with the free surface boundary blocking effect, this process causes asymmetric behavior of turbulent intensity and length scales in all three directions. Therefore, one of the goals of the present work is to conduct laboratory and numerical investigations in which these processes are explored and quantitative results are provided for validation of present and future theoretical models.

[8] Following *Veron and Melville* [2001], who adopted the use of the active thermography technique (previously used for air-sea gas transfer studies [e.g., *Haussecker et al.*, 1998]), for turbulent velocity measurements at the water surface, we employ a similar technique in the present experiment, described in section 2.2. Given the recent improvements in infrared vision technology, we believe this approach yields better signal-to-noise ratio, and provides easier access to the near-surface velocities compared to alternative methods (i.e., Particle Image Velocimetry [e.g., *Babanin and Haus*, 2009]). The numerical model is briefly described in section 2.3, for more detailed description the reader is referred to a companion paper by *Babanin and Chalikov* [2012]. Both experimental and numerical results are presented and discussed in section 3.

2. Methodology

2.1. Facility Description

[9] The experiments were performed in the Free Surface Hydrodynamics Lab at the Naval Research Lab in Washington, DC. The wave tank (see Figure 1) is approximately 8.5 m long and 2.3 m wide with 0.75 to 0.9 m high walls. Side and bottom surfaces are clear glass panels. The wave maker, which takes up about 1 m of the tank length, is a wet-backed paddle actuated by a computer-controlled servo motor. The wave maker paddle is a rigid aluminum plate spanning the entire width of the tank and produces highly two-dimensional waves. Water depth was 0.5 m for all tests. Salt water was used for these experiments (fresh water mixed with Instant Ocean sea salt mix) though it is believed that fresh water would yield similar results. To minimize the effect of surfactants, the water was filtered daily with a diatomaceous earth filter (5 μm particle size) and a surface skimmer.

[10] Waves were generated via sinusoidal motions of the wave paddle. For each wave packet, amplitude (i.e., paddle stroke) was linearly increased from zero to a constant value over a period of 6.7 s. The amplitude was then held constant for 6 s and then linearly decreased back to zero over a period of 1 s. This particular wave packet shape was optimized for the dimensions of the wave tank. On one hand, the ramp-up

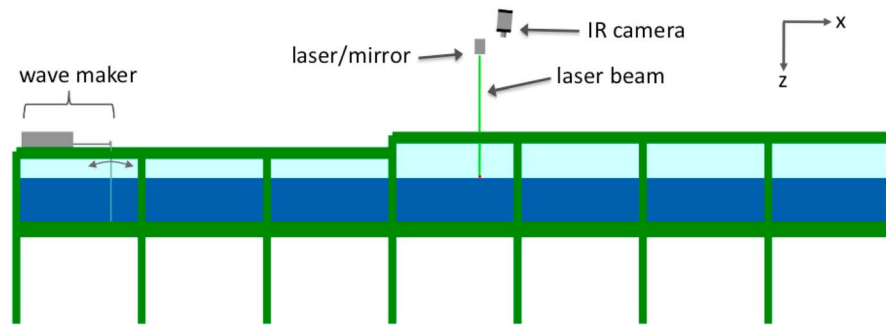


Figure 1. Schematic illustration of wave tank and experimental setup. Tank dimensions are 8.5 m long by 2.3 m wide with 0.75–0.9 m high sidewalls. The test area is located 3.6 m from the wave maker and 4.0 m from the back wall.

time needed to be minimized in order to increase the useful test time until the first reflected wave comes back from the far end of the tank. On the other hand, if the ramp-up time is short and the wave steepness is high, the wave energy tends to concentrate at the leading edge of the wave packet and cause unwanted wave breaking. The chosen ramp-up time (6.7 s) is a trade-off, resulting in a quick amplitude runup ($\sim 1\text{--}3$ s, depending on wave period and steepness) at the test area location, followed by a series of 6–9 wave periods with nearly constant wave amplitude. This amplitude was measured by a capacitance elevation gauge (RBR WG-50) and used in the data analysis below.

2.2. Thermal-Marking Velocimetry

[11] Thermal-marking velocimetry (TMV) is a type of active thermography first described by *Veron et al.* [2008]. The basic premise is to use actively heated points on the water surface as tracers in order to visualize and quantify the

surface flow. It is similar to particle image velocimetry (PIV) in that image pairs are used to calculate tracer displacements and thus flow field velocities by dividing displacement by the time step between image pairs. Thermal markers have the advantage of being minimally invasive to the flow (the depth of heating is on the order of $10\ \mu\text{m}$), easily identifiable, renewable and configurable.

[12] Figure 2 illustrates the general procedure. In Figure 2a, the beam from a laser is directed via a mechanized mirror to a point on the water surface for a brief period of time, Δt . During that time, the beam heats the water surface to a slightly higher temperature than ambient. The mirror then redirects the beam to a second point for the same period of time. This continues along a straight line to create a series of thermal markers, as shown in Figure 2b, also referred to as a scan. Once a scan has been laid down, an image is recorded by an overhead IR camera. A second IR image is recorded later to assess the displacement of each marker

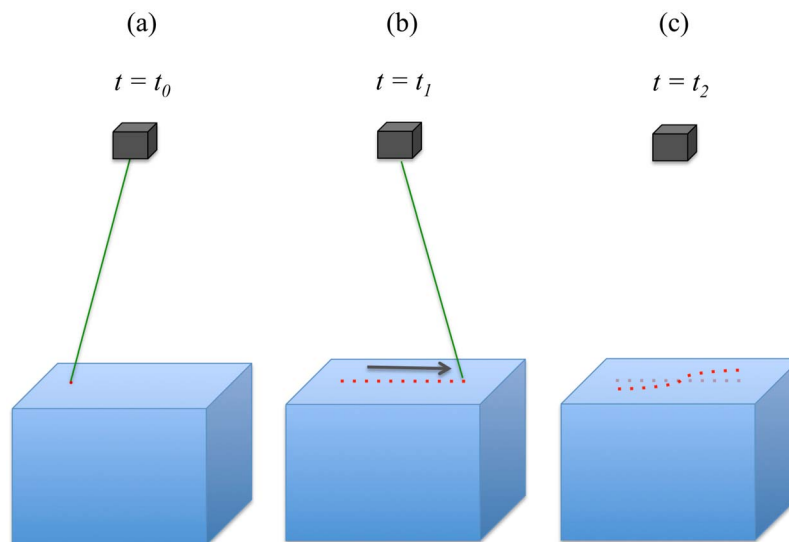


Figure 2. Overview of TMV setup. (a) A laser beam is directed to a point on the water surface for a brief period of time, heating it to a higher temperature than ambient. (b) The laser beam is redirected to another point and the process is repeated to create a series of warm points, called thermal marks, on the surface. (c) If a flow field is present at the water surface, the line of thermal marks will be distorted and the displacement of individual marks can be used to deduce the flow field. In the present study, a line of 38 thermal marks with a spacing of 0.6 cm are produced during each laser scan.

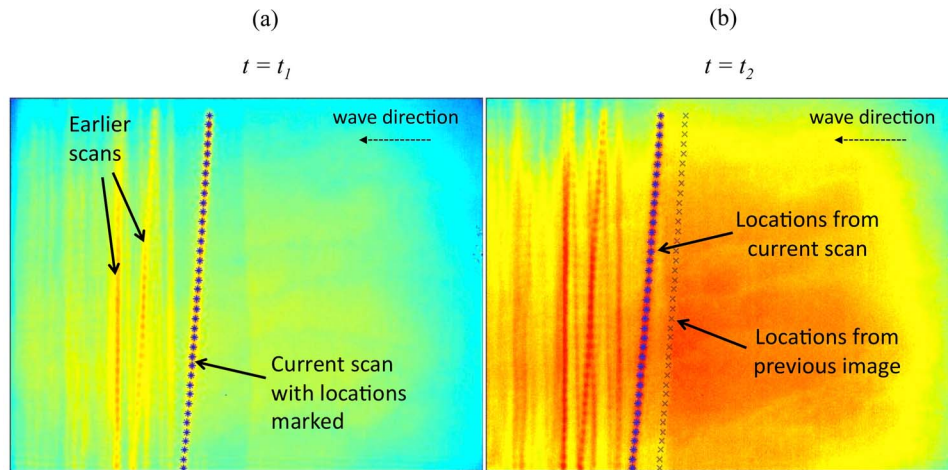


Figure 3. Sample IR images from TMV experiment with t_1 and t_2 corresponding to Figure 2. (a) The first image is taken immediately after a scan of thermal marks is laid down. (b) The second image is taken 38 ms later (each image has a 2 ms exposure), with the prior thermal mark locations also shown. The orientation of the laser scan is perpendicular to the wave direction, which is from right to left in the image. Field of view is approximately 31 cm by 25 cm for each image. Note that contour shading is scaled according to the temperature range over the entire image, which is typically about 1.5°C .

which, by dividing the displacement by the time elapsed between images, is used to deduce the local surface velocity field during that time step, as illustrated in Figure 2c.

[13] In the present study, a 10 watt CO_2 laser (SYNRAD 48-1 laser with $10.2\text{--}10.8\ \mu\text{m}$ wavelength, UC-2000 controller) was positioned above the tank and oriented horizontally. The full power beam was redirected downward to the water surface with a controllable mirror (General Scanning Inc. CX-660). The mirror was located 175 cm above the water surface. A germanium focusing lens was placed between the laser and the mirror, located adjacent to the mirror. The IR camera (FLIR SC6000) detects midwave IR signals ($3\text{--}5\ \mu\text{m}$ wavelength). The camera was positioned 195 cm above the water surface at a slight angle ($\sim 7^\circ$) from vertical (this is done to minimize self-reflection on the water surface). The image area, which is approximately $25\ \text{cm} \times 31\ \text{cm}$, is about 360 cm downstream from the wave maker, 70 cm from the nearest sidewall and 400 cm from the back wall of the tank. A capacitance elevation gauge was located 50 cm away (toward the left sidewall) at the same longitudinal position as the test area.

[14] Based on the laser wavelength range and published values of Lambert absorption coefficient [see *Downing and Williams*, 1975], the laser intensity is 90% attenuated at a depth of 10 to $14\ \mu\text{m}$. The IR camera wavelength range has a similar average absorption coefficient as the laser and has an average depth of penetration (using 90% attenuation) of about $10\ \mu\text{m}$, though this ranges between $0.9\ \mu\text{m}$ and $90\ \mu\text{m}$ within the camera wavelength range. These depths are all considerably less than a typical thermal boundary layer of 1 to 30 mm [Veron and Melville, 2001].

[15] Camera and lens (25 mm, indigo) calibration was performed using a temperature-controlled black body. Images were taken of the body at specific temperatures between 20 and 30°C . The lens was positioned 1 m from the body during calibration and a 2 ms integration time was used.

Each pixel recorded by the camera contains a numeric value corresponding to measured temperature. These values were averaged over the field of view for each temperature and plotted versus temperature. The slope of a line fitted to these points yields a calibration constant of 255.97°C across the temperature range. The r^2 value of this fit is 0.9985 which corresponds to a standard deviation of about 0.06°C .

[16] A duration of 1 ms was used for each thermal mark and there were a total of 38 points, thus each scan took 38 ms to complete. The laser scan was oriented nearly parallel to the wave crest, or perpendicular to the wave direction. The individual marks are on the order of 0.5 cm in diameter and are spaced approximately 0.6 cm to minimize overlapping. Maximum temperature of each mark was typically about 1°C higher than the ambient temperature. The laser was on throughout the scan (i.e., 38 ms continuous pulse) with the mirror moving to each new location every 1 ms (the mirror movement is quite fast—on the order of microseconds). The laser is off during the period between the scans. The first image was taken 1 ms after scan completion and had a 2 ms exposure time. The second image was taken 38 ms after the completion of the first image and also used a 2 ms exposure time. The next scan began while the second image was being taken such that a new scan was started every 80 ms and an image was taken every 40 ms. There is a slight time lag of about 1 ms in the laser system for each pulse which prevents spillover between the second image and the start of the next scan. A central computer was used to synchronize all aspects of the experiment including the wave maker motion and camera/laser timing.

[17] A pair of sample IR images are shown in Figure 3. The locations from Figure 3a are marked on both images to illustrate the displacement of the thermal marks on Figure 3b. Marks from previous scans, which are visible in both images, tend to accumulate downstream of the test area due to Stoke's drift. Precise thermal mark locations were determined using

a numerical search algorithm that uses a weighted centroid calculation for each marker to achieve subpixel accuracy. Approximate marker locations are first identified by searching for high-temperature regions near the top and bottom of the image, fitting a straight line and dividing the line into 38 points. These approximate locations are then used as starting points for an iterative process that locates the weighted centroid of the area local to the starting point, updating the starting point with each iteration. The initial calculation area typically covers the entire thermal mark, which is about 10 pixels in diameter, and is slightly reduced during subsequent iterations. Because the thermal markers dissipate rather quickly, the highest temperature regions of each image reliably corresponded to the most recent scan. Occasional errant marker locations (about 1% of all points) were easily identified visually and corrected. Based on tests conducted using still water (i.e., zero surface velocity and thus zero displacement between images), marker tracking accuracy was determined to be within 0.034 pixels, which is similar to the reported accuracy of 0.05 pixels in *Veron et al.* [2008]. Using images of a ruler in the field of view, the length scale was determined to be 20.48 pixels per cm which was assumed to be approximately constant in both directions throughout the image and at all surface elevations. This value corresponds to a location measurement accuracy of 0.0017 cm. The velocity accuracy is therefore $2 \cdot 0.0017 \text{ cm} / 40 \text{ ms} = 0.084 \text{ cm/s}$ (the factor of 2 is used because two images are used for each velocity calculation). Increasing the period between scans improves the velocity measurement accuracy but decreases the sampling rate. It should be noted that the passing waves will result in curved surfaces with varying distances from the camera. Because relatively small amplitude waves (up to 6 cm wave height) were used in this study, the velocity error due to these effects is estimated to be less than $\pm 1.5\%$. This will later be shown to be negligible compared to the range of turbulence magnitudes measured throughout a given wave cycle. Images were taken during the entire duration of each run but the processed portion of the data only included fully developed waves before any reflected waves returned to the test area. This typically resulted in 6–9 individual waves for each test. Surface elevation data were inspected to ensure that processed data did not include any reflected waves, which were very easy to identify in the data.

2.3. Numerical Model

[18] The model represents the development of approach formulated by *Benilov and Lozovatskiy* [1977] and initiated by experimental data of *Babanin and Haus* [2009]. The calculations were made with a Large Eddy Simulation (LES) model of 3-D nonpotential (vortical) motion coupled with a 2-D model of surface waves [*Chalikov and Sheinin*, 1998]. The equations are written in cylindrical conformal coordinates. The equations of vortical flow are derived as follows (see details in *Babanin and Chalikov* [2012]): (1) all variables are represented as sum of potential and nonpotential components, (2) equations for vortical motion in Cartesian coordinate system are obtained by extraction of the 2-D potential flow equations from initial Euler equations, (3) the equations for vortical flow are averaged over 3-D cells for separation of individually described motion and subgrid

turbulence, and (4) averaged equations for vortical motion are transferred into conformal cylindrical coordinate system.

[19] Finally the equations for vortical motion take the form

$$\frac{dJu_x}{d\tau} = -\omega^\vartheta W - x_\xi \Pi_\xi + z_\xi \Pi_\xi + F_\xi, \quad (3)$$

$$\frac{dJu_y}{d\tau} = -\omega^\zeta U + \omega^\xi W - J\Pi_\vartheta + F_\vartheta, \quad (4)$$

$$\frac{dJu_z}{d\tau} = \omega^\vartheta U - z_\xi \Pi_\xi - x_\xi \Pi_\zeta + F_\zeta. \quad (5)$$

[20] Here τ is a time, ξ , ϑ , and ζ are the conformal coordinates, u_x , u_y , u_z are velocity components of vortical motion, ω^ξ , ω^ϑ , ω^ζ are vorticity components multiplied by Jacobian J ; U and W are orbital velocities of potential flow calculated with equation for potential waves, x_ξ and z_ξ are metric coefficients; Π is generalized pressure

$$\Pi = p + u_x U + u_z W + \frac{2}{3}e, \quad (6)$$

where e is the kinetic energy of subgrid turbulence, and F_ξ , F_ϑ , and F_ζ denote the sums of advection and turbulent terms. The terms including the components of vorticity describe the momentum transfer from potential waves to vortical motion. Since the energy of vortical motion is much smaller than the energy of the waves, the back transfer of energy to waves and attenuation of waves due to dissipation are not presently taken into account. The equations for potential waves and for vortical motion are integrated in time using a Runge-Kutta time scheme and the one iteration time scheme correspondingly.

[21] Initial conditions were assigned as a train of four harmonic waves using small amplitude theory. Initial turbulence was introduced as a field of random velocities satisfying the continuity equation. Total initial turbulent energy was set equal to 0.001 of the total wave energy. Using the periodic boundary condition, waves were allowed to propagate for the duration of up to 10 wave periods. Note that in high wave steepness cases waves quickly developed nonlinear instabilities and the calculations had to be stopped ahead of time to prevent the occurrence of micro breaking (see *Babanin et al.* [2010] for detailed description of this effect).

3. Results and Discussion

3.1. Overall Growth of TKE in Time

[22] A total of 28 cases were tested experimentally, including 5 different wave periods with varying amplitudes (see Table 1). Wave periods were chosen to be integer multiples of the 80 ms sampling interval (i.e., $T = 0.64, 0.72, 0.80, 0.88, \text{ and } 0.96 \text{ s}$). This aided in the investigation of correlation between surface velocities and wave phase, because the wave phases at which the velocities were measured remained consistent throughout the wave packet. By means of the TMV technique, each of the 38 thermal markers yields an individual realization of surface velocity (e.g., Figure 4) along a nearly constant wave phase every 80 ms.

Table 1. Summary of Input Parameters and Measured Properties

Run	Wave Period T (s)	Wave Number k (m) ⁻¹	Wave Steepness ak	x Turbulent Growth Rate ^a	y Turbulent Growth Rate ^b	Wave Energy ^c (cm/s) ²	Eddy Size L_{eddy} (cm)
661	0.96	4.47	0.077	0.006	0.14	91	10.7
660	0.96	4.47	0.095	-0.063	0.31	128	8.8
659	0.96	4.47	0.112	-0.018	0.164	172	7.6
658	0.96	4.47	0.130	-0.046	0.141	221	9.5
657	0.96	4.47	0.145	-0.034	-0.026	272	8.2
656	0.96	4.47	0.159	0.021	0.055	321	7.6
667	0.88	5.26	0.096	-0.009	0.068	111	6.93
666	0.88	5.26	0.118	0.048	0.057	154	8.2
665	0.88	5.26	0.137	0.172	0.203	210	8.2
664	0.88	5.26	0.159	0.074	0.288	274	6.3
663	0.88	5.26	0.179	0.084	0.23	347	5.7
662	0.88	5.26	0.202	0.097	0.153	441	6.9
640	0.8	6.32	0.136	0.096	0.182	153	7.6
639	0.8	6.32	0.164	0.049	0.119	225	8.2
638	0.8	6.32	0.190	0.115	0.311	295	6.3
637	0.8	6.32	0.210	0.144	0.426	381	5.7
636	0.8	6.32	0.234	0.163	0.181	484	5.7
635	0.8	6.32	0.265	0.208	0.172	626	6.3
644	0.8	6.32	0.284	0.204	0.258	663	5.7
671	0.72	7.78	0.152	0.06	-0.01	184	6.3
670	0.72	7.78	0.194	0.22	0.214	275	6.9
669	0.72	7.78	0.226	0.16	0.14	384	6.9
668	0.72	7.78	0.259	0.053	0.015	525	7.6
649	0.64	9.83	0.111	-0.003	0.1	104	7.6
648	0.64	9.83	0.145	0.055	0.085	166	8.8
647	0.64	9.83	0.190	0.049	0.215	230	8.2
645	0.64	9.83	0.224	0.176	0.258	307	6.9
646	0.64	9.83	0.263	0.056	0.171	382	8.2

^aDefined as $\frac{\partial u_x^2 / u_{x0}^2}{\partial t / T}$.

^bDefined as $\frac{\partial u_y^2 / u_{y0}^2}{\partial t / T}$.

^cDefined as $\langle U_x^2 \rangle$.

The average x component velocity of the 38 measurements was considered to be the wave orbital velocity, U_x . In order to obtain the turbulent velocity component, the finite time of each scan had to be considered. The scan tilt, visible in Figure 3, is present due to the horizontal surface displacement during the scan. As a result, there is a small difference between the wave phase, and thus orbital velocity within the set of 38 markers. This difference in orbital velocity has to be accounted for before the turbulent velocity component can be separated. It was found that a linear fit is sufficient to account for this effect, as shown in the example on Figure 4. The linear fit was subtracted from each set of measured velocities, thus providing 38 measurements of turbulent velocities u_x and u_y , at every time step.

[23] Because of the physical limitation of 6 to 9 wave periods for each run, statistical uncertainties become very important to the data analysis. Even though thousands of velocity measurements were made during each run, turbulent growth rates were found to differ significantly for seemingly similar conditions (e.g., runs 635 and 644 (Table 1)). There are multiple potential reasons for this variability including measurement errors, sensitivity to a fluctuating time of the turbulence initiation, and velocity fluctuations on long timescale. Therefore, to increase statistical confidence, the analysis is structured in such a way that data from all runs are used to calculate each result, without having to rely on results from individual runs. To some extent this requirement limits the ability to make correlations between individual wave parameters and turbulence production.

[24] In the beginning of the data analysis, it is important to confirm with the highest possible certainty that turbulence is indeed being produced. Therefore, the temporal evolution of turbulent kinetic energy, i.e., u_x^2 and u_y^2 , across all 28 runs is

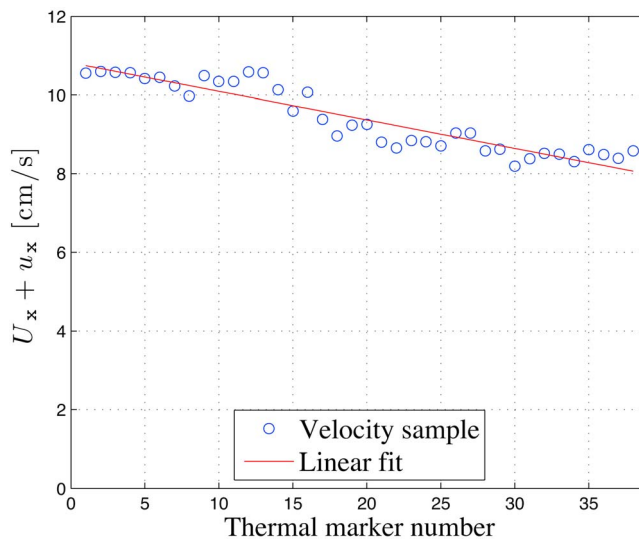


Figure 4. An example of raw surface velocities, corresponding to 38 thermal markers within one scan. Each velocity realization contains both orbital U_x and turbulent u_x components.

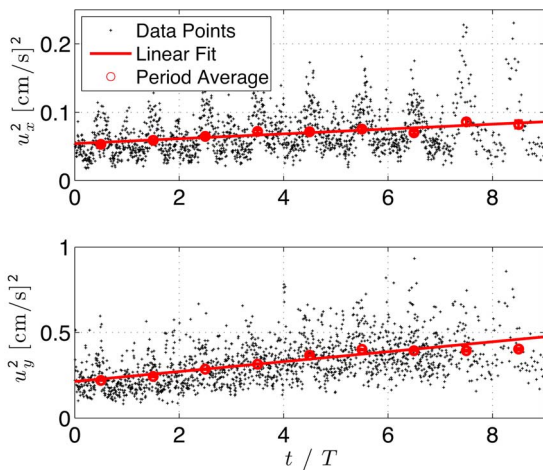


Figure 5. Turbulent components of the surface velocities u_x^2 and u_y^2 are shown as functions of nondimensional time t/T for the entire data set. Each point is a bin average over 50 realizations, the solid line is a linear fit through all realizations, and circles with 95% confidence intervals are averages over each wave period.

shown in Figure 5. Each data point represents a bin average over 50 measurements, the solid line shows a linear fit over all data, and the circles are averages for each wave period with corresponding 95% confidence intervals. Bin averages over each wave period clearly indicate that the growth of turbulent intensity indeed takes place in both the x and y directions. Results of the numerical simulations, presented in the following sections, suggest similar positive trends. Note that quantitative comparison of experimental and numerical results is premature at this point because of the expected strong dependence on the initial TKE. An arbitrary level of TKE was introduced in the numerical simulations (both present, as well as *Teixeira and Belcher* [2002]) as an initial condition. In the experiments, however, the TKE was allowed to occur naturally. Therefore, the absolute values of turbulence intensity in the laboratory and in the numerical simulations are not expected to match.

[25] In spite of the quantitative uncertainty resulting from the treatment of initial TKE, several interesting findings were observed. One such finding is that the value of u_y^2 is greater than the value of u_x^2 by a factor of 4 or more, which implies strong horizontal anisotropy of the turbulence at the surface. This anisotropy is also predicted by our numerical simulations (as will be shown in Figure 7), as well as by *Teixeira and Belcher* [2002], who attribute it to the horizontal stretching of vorticity by the Stokes drift shear. This mechanism is expected to produce elongated eddies with the vorticity oriented in the wave propagation direction (streamwise). Thus, the streamwise turbulent energy is transferred to spanwise and vertical components. However, *Teixeira and Belcher* [2002] predicted a decay of streamwise turbulence in time, whereas the present experimental and numerical simulations find positive growth (see section 3.4). There are a number of possible explanations for this discrepancy. First, it is reasonable to hypothesize that u_x^2 will eventually reach an equilibrium where its production is equal to

dissipation plus transfer to u_y^2 and u_z^2 . Therefore, if the initial intensity of streamwise turbulence, i.e., u_{x0}^2 , was set above the saturation level, u_x^2 would decay, whereas the experiments start with nearly quiescent fluid, therefore u_x^2 grows. This hypothesis could be tested in future studies by varying initial TKE either numerically or experimentally. Another possibility involves an additional source of vorticity due to some high-order nonlinear effects [e.g., *Longuet-Higgins*, 1992] not accounted for in numerical simulations of *Teixeira and Belcher* [2002]. More evidence for the possible importance of such mechanism is revealed below in the analysis of dependencies on wave phase and wave steepness.

3.2. TKE Dependence on Wave Phase

[26] In addition to overall growth, theoretical predictions by *Teixeira and Belcher* [2002] suggested TKE dependence on wave phase. To investigate this effect further the following steps were taken. First, within each run a spline curve was fitted through wave orbital velocity data points, and the wave phase was calculated by means of a Hilbert transformation. Second, within each run orbital velocities were averaged for each wave phase to reconstruct the shape of an average wave within the packet. Third, using the wave phase information, averaged phase dependences of turbulent components u_x^2 and u_y^2 were constructed for each run and then averaged over all runs. The results are shown in Figure 6, where two identical periods are shown for visualization purposes. A clear peak is visible in streamwise turbulence intensity, u_x^2 , at the wave crest, and a similar peak is visible in the y direction, though not as distinct.

[27] Our numerical results were obtained in a similar way, using the output data of the numerical model (Figure 7). The model also predicts a spike of TKE at the wave crest. Here the turbulent velocities u_{xn} , u_{yn} , and u_{zn} are normalized by

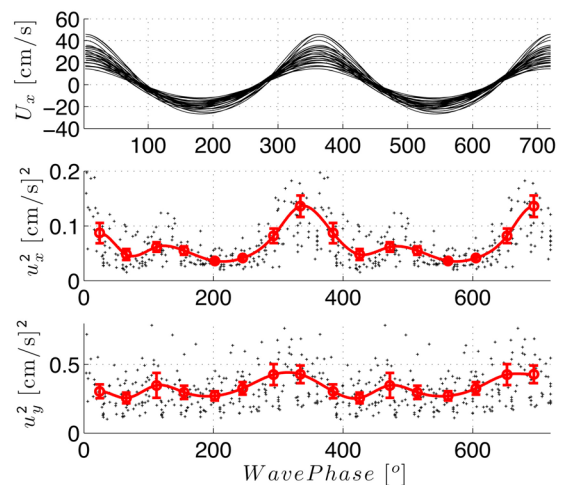


Figure 6. (top) Each of the 28 curves (corresponding to the 28 runs (see Table 1)) represents an averaged dependence of wave orbital velocity on the wave phase. (middle and bottom) Data points are average values obtained from individual runs, circles with 95% confidence intervals are 45° bin averages over the data points, and the solid line is a spline fit through the bin averages. For visualization purposes, all three plots show a sequence of two identical wave periods.

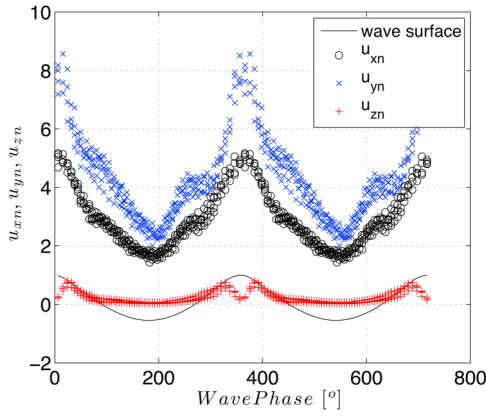


Figure 7. Numerical simulation of normalized turbulent velocities, defined in equation (7), shown as functions of wave phase. Solid line corresponds to the normalized wave-shape, with wave steepness at $ak = 0.167$.

the significant wave height H_s and orbital wave frequency ω as

$$u_{xn} = \frac{\langle u_x^2 \rangle^{0.5}}{H_s \omega}, u_{yn} = \frac{\langle u_y^2 \rangle^{0.5}}{H_s \omega}, u_{zn} = \frac{\langle u_z^2 \rangle^{0.5}}{H_s \omega}. \quad (7)$$

[28] The peak of TKE near the wave crest appears at all wave steepnesses in our numerical simulations. Interestingly, turbulence stays nearly isotropic horizontally at low wave steepness, but then the ratio u_{yn}/u_{xn} rapidly grows around $ak = 0.15$ and eventually settles above 2 to match the experimental results (see section 3.1). As expected, the vertical component u_{zn} is suppressed due to proximity to the free surface, therefore its magnitude is much smaller.

[29] In contrast, the numerical simulations by *Teixeira and Belcher* [2002, 2010] produced phase-dependent functions that differ significantly from our experimental and numerical results. Although in their simulations u_x has its peak at the wave crest, the total TKE maximum is found at the wave trough. Perhaps the nonlinear effects in the wave crest region [e.g., *Longuet-Higgins*, 1992] that are not captured by their model are dominating in the range of wave steepness investigated in our study. Also note that, unlike our model, *Teixeira and Belcher* [2002] retains the vertical turbulent component near the water surface, approximating the blocking effect of the free surface boundary in the postprocessing stage as

$$\left(u_x^2 + u_y^2 + u_z^2 \right) \Big|_{z \rightarrow \infty} = \left(u_x^2 + u_y^2 \right) \Big|_{z=0}. \quad (8)$$

This simplification has unknown consequences and may be suggested as a source of deviation from our experimental results. Additionally, a recent detailed direct numerical simulation study on the subject by *Guo and Shen* [2010] revealed more complex dynamics of near-surface turbulence. Therefore, it is suggested that the assumption stated in equation (8) should be revisited in future studies, given the strong anisotropy of the surface turbulence.

3.3. Turbulent Length Scale

[30] Qualitative structure of the elongated near-surface eddies can be seen in Figure 8, which shows an example of a

raw infrared image. In addition to the thermal markers, the infrared image shows a series of cold and warm streaks in the direction of wave propagation (right to left). As a possible explanation of the observed structure, it is suggested that the cold streaks might correspond to convergence zones of the surface skin layer, cooled by evaporation. If so, mass conservation also dictates that the cold streaks correspond to downward motion, whereas wider warm streaks correspond to regions of upward motion of warmer subsurface water. Another notable feature exposed by the thermal markers is the acceleration of the downstream surface flow around the narrow cold streaks which deforms the lines of thermal marks as they propagate downstream. It should be noted that these streaks were only observed in a few test cases and may be related to the presence of convection cell structures, which is primarily dependent on evaporation rate and surfactant concentration, prior to each test run.

[31] Normalized autocorrelation functions were used to quantify length scales of the observed eddies:

$$R_x(r) = \frac{\langle u_x(y)u_x(y+r) \rangle}{\langle u_x^2 \rangle}, \quad (9)$$

$$R_y(r) = \frac{\langle u_y(y)u_y(y+r) \rangle}{\langle u_y^2 \rangle}. \quad (10)$$

The functions were calculated for each scan and then averaged over all scans within each run. In Figure 9 the resulting data points are shown as a function of distance, r , and the solid line represents the autocorrelation function averaged over all runs. The distance at which the autocorrelation function has the first minimum is assumed to be the size of the dominant eddy, L_{eddy} , in y direction. In Figure 10 L_{eddy} , calculated separately for each run based on its R_x (which resulted in a more pronounced minimum), is shown as a

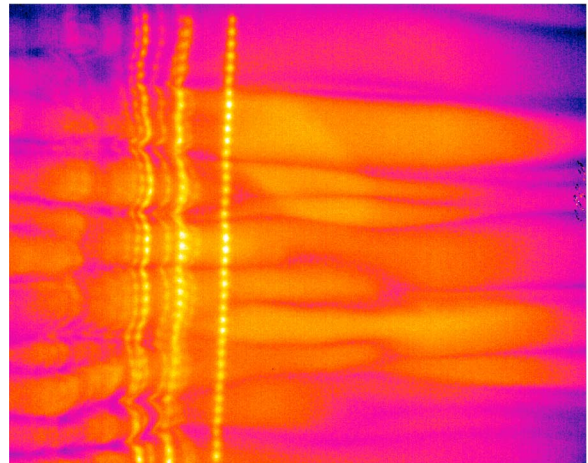


Figure 8. An example of a raw infrared image of the water surface with observed thermal streaks. Waves are propagating from right to left. Image brightness represents water temperature, ranging within $\sim 1^\circ\text{C}$. The image area is approximately 25×31 cm. Vertical bright dotted lines are thermal markers, and horizontal streaks correspond to elongated near-surface eddies.

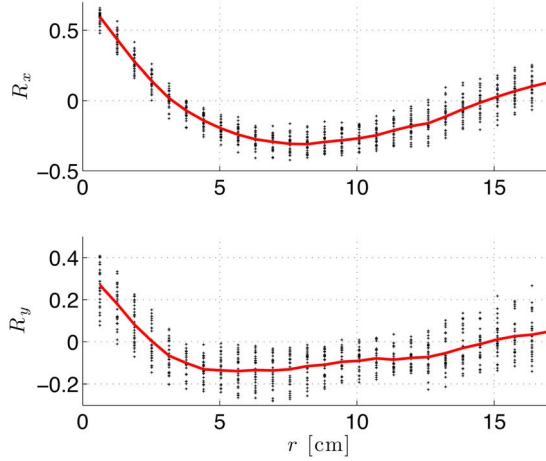


Figure 9. Normalized autocorrelation functions based on u_x and u_y measurements. Data points are averages over all data within individual runs corresponding to a specific distance r . Solid curves are autocorrelation functions averaged over entire data set.

function of corresponding wave steepness ak . An attempt was made to find dependences of L_{eddy} on other parameters, such as wave phase or normalized time, but no statistically significant correlation was found. Moreover, the large scatter in the data does not allow for more detailed nondimensional length scale analysis, but it does appear that L_{eddy} decreases with increasing wave steepness.

3.4. Nondimensional TKE Growth Rate

[32] Predictions of our numerical model, the model by [Teixeira and Belcher, 2002], as well as observations by Veron *et al.* [2009] suggest that the turbulent growth rate increases with wave steepness. But surprisingly the correlation between $\partial u_x^2 / \partial(t/T)$ or $\partial u_y^2 / \partial(t/T)$ and ak was found to be weak and statistically insignificant within the present laboratory data set. While the experimental noise likely contributes to the weak correlation, it is also possible that there is a more dominant controlling parameter besides wave steepness. Recalling equation (1), turbulence production is not only a function of wave steepness, which controls the Stokes drift gradient term, $\partial U_x / \partial z$, but also the Reynolds stress. It is possible that the variation of the initial Reynolds stress within our data set is larger than the variation of wave steepness, causing the scatter in the TKE versus ak dependence. But since the vertical turbulent velocities were not measured, the value of the Reynolds stress is unknown. Instead, as in Teixeira and Belcher [2002], the initial turbulent kinetic energy is implemented as a normalization parameter, i.e., u_{x0}^2 and u_{y0}^2 . Although not ideal, this removes some of the scatter and reveals the dependence of the normalized TKE growth rate, i.e.,

$$P_x = \partial(u_x/u_{x0})^2 / \partial(t/T), \quad (11)$$

$$P_y = \partial(u_y/u_{y0})^2 / \partial(t/T), \quad (12)$$

on the wave steepness (see Figure 11). Interestingly, while the growth of u_y^2 is already high at $ak \approx 0.1$ and only slightly

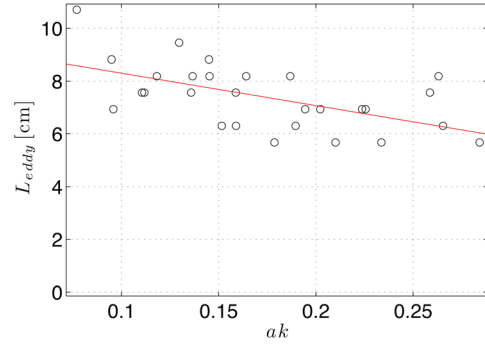


Figure 10. The dominant eddy length scale in the y direction is shown as a function of wave steepness.

increases toward higher wave steepness, the growth of u_x^2 is small or even negative around $ak \approx 0.1$, but quickly grows and becomes similar to the u_y^2 growth at the highest wave steepness. For lower wave steepness, these findings are in agreement with the mechanism described by Teixeira and Belcher [2002], in which u_x^2 does not grow due to the $u_x^2 \rightarrow u_y^2$ energy flux. However, apparently at higher steepness other turbulence production mechanisms begin to be important, which makes turbulent growth more isotropic. It is also possible that the same mechanisms add smaller-scale turbulent motion to the existing elongated eddies (e.g., Figure 8), and therefore are responsible for the spanwise length scale decrease at high wave steepness (see Figure 9).

[33] Figure 11 also shows the growth rate of overall TKE, i.e., q^2 , obtained numerically. Here the relative growth rate was defined as a ratio of TKE of the current wave period to the TKE of the previous wave period, averaged over the entire duration of a run. While the result agrees with experimental data at lower wave steepness, after ak exceeds 0.18, numerical simulations start encountering Benjamin-Feir type wave instabilities, which lead to a rapid increase in turbulence production. This effect was described in detail

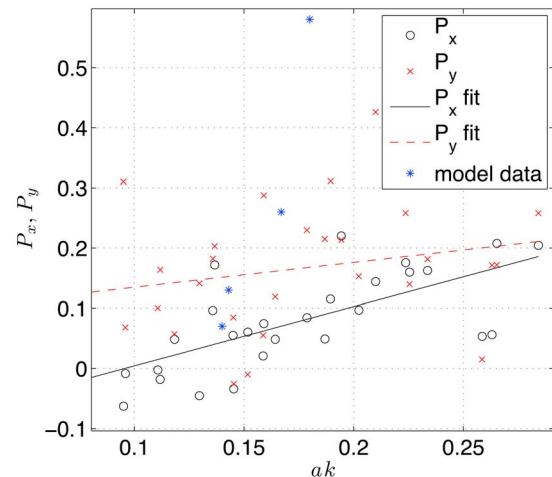


Figure 11. The growth rates of u_x^2 and u_y^2 as measured experimentally are shown with open circles and crosses, whereas the growth of total normalized TKE as found in numerical simulations is shown with asterisks.

by Babanin *et al.* [2010]. The same instability was not observed experimentally likely because the waves were not allowed to propagate long enough to develop sufficient nonlinearity.

4. Conclusions

[34] An investigation of moderately steep monochromatic waves was undertaken to explore the mechanisms of initial wave-induced turbulence production and subsequent wave-turbulence interaction. For this purpose, surface velocities were measured in a laboratory wave tank with high precision using the TMV technique. Turbulent fluctuations were decoupled from the wave orbital velocities, followed by the assessment of dependencies of turbulent properties on normalized time, wave phase, and wave steepness. Similar dependencies were sought in a parallel numerical simulation investigation.

[35] In both numerical and laboratory simulations the turbulent kinetic energy (TKE) was found to grow in time, due to the wave-turbulence interaction. Moreover, TKE dependence on wave phase, as well as the turbulent anisotropy near the surface were revealed and found to match between the experimental and numerical results. The present experiment also confirmed the existence of near-surface eddies, elongated in the streamwise direction. The spanwise length scale of these eddies appeared to decrease with increasing wave steepness, however no evidence was found for any length scale dependence on wave phase or time.

[36] In agreement with present and some past numerical investigations, this experiment indicates that the turbulence production rate is highly sensitive to the initial conditions of the turbulence. To account for this dependence, the turbulent growth is normalized by the initial TKE, which appears to be a simplified proxy of a more complex normalization parameter. Hence, further studies are needed to investigate the dependence of the TKE growth rate on initial values of TKE, Reynolds stress, turbulence directionality, and length scales. Also, present analysis exposes a need to explore the possibility of the existence of an equilibrium state for the streamwise component of TKE, in which its production might be balanced by the energy transfer to spanwise and vertical components, as well as dissipation.

[37] **Acknowledgments.** The authors would like to thank Glenn Frick for his invaluable assistance with the experimental setup, as well as acknowledge Alex Babanin for his contribution to the development of the numerical model and for raising awareness of the wave-induced turbulence problem.

References

Ardhuin, F., and A. Jenkins (2006), On the interaction of surface waves and upper ocean turbulence, *J. Phys. Oceanogr.*, *36*, 551–557.

- Babanin, A. (2006), On a wave-induced turbulence and a wave-mixed upper ocean layer, *Geophys. Res. Lett.*, *33*, L20605, doi:10.1029/2006GL027308.
- Babanin, A., and D. Chalikov (2012), Numerical investigation of turbulence generation in nonbreaking potential waves, *J. Geophys. Res.*, doi:10.1029/2012JC007929, in press.
- Babanin, A., and B. Haus (2009), On the existence of water turbulence induced by nonbreaking surface waves, *J. Phys. Oceanogr.*, *39*, 2576–2679.
- Babanin, A., D. Chalikov, I. Young, and I. Savelyev (2010), Numerical and laboratory investigation of steep two-dimensional waves in deep water, *J. Fluid Mech.*, *644*, 433–463.
- Benilov, A., and I. Lozovatskiy (1977), Semi-empirical methods of the turbulence description in the ocean, in *The Turbulent Diffusion of the Ingressants in the Sea, Inf. Bull.* *5*, pp. 89–97, Coord. Cent. of COMECON, Moscow.
- Chalikov, D., and D. Sheinin (1998), Direct modeling of one-dimensional nonlinear potential waves, in *Nonlinear Ocean Waves, Adv. Fluid Mech.*, vol. 17, edited by W. Perrie, pp. 207–258, WIT, Southampton, U. K.
- Cheung, T., and R. Street (1988), The turbulent layer in the water at an air-water interface, *J. Fluid Mech.*, *194*, 133–154.
- Craik, A., and S. Leibovich (1976), A rational model for Langmuir circulations, *J. Fluid Mech.*, *73*(3), 401–426.
- Dai, D., F. Qiao, W. Sulisz, L. Han, and A. Babanin (2010), An experiment on the nonbreaking surface-wave induced vertical mixing, *J. Phys. Oceanogr.*, *40*, 2180–2188.
- Downing, H., and D. Williams (1975), Optical constants of water in the infrared, *J. Geophys. Res.*, *80*(12), 1656–1661.
- Drennan, W., M. Donelan, E. Terray, and K. Katsaros (1997), On waves, oceanic turbulence, and their interaction, *Geophysica*, *33*(2), 17–27.
- Guo, X., and L. Shen (2010), Interaction of a deformable free surface with statistically steady homogeneous turbulence, *J. Fluid Mech.*, *658*, 33–62.
- Haussecker, H., U. Schimpf, and B. Jähne (1998), Measurements of the air-sea gas transfer and its mechanism by active and passive thermography, in *IEEE International Geoscience and Remote Sensing Symposium Proceedings*, vol. 1, pp. 484–486, Inst. of Electr. and Electr. Eng., Piscataway, N. J.
- Huang, C. J., and F. Qiao (2010), Wave-turbulence interaction and its induced mixing in the upper ocean, *J. Geophys. Res.*, *115*, C04026, doi:10.1029/2009JC005853.
- Longuet-Higgins, M. (1992), Capillary rollers and bores, *J. Fluid Mech.*, *240*, 659–679.
- McWilliams, J., P. Sullivan, and C.-H. Moeng (1997), Langmuir turbulence in the ocean, *J. Fluid Mech.*, *334*, 1–30.
- Milgram, J. (1998), Short wave damping in the simultaneous presence of a surface film and turbulence, *J. Geophys. Res.*, *103*, 15,717–15,727, doi:10.1029/98JC01191.
- Phillips, O. (1961), A note on the turbulence generated by gravity waves, *J. Geophys. Res.*, *66*(9), 2889–2893.
- Teixeira, M., and S. Belcher (2002), On the distortion of turbulence by a progressive surface wave, *J. Fluid Mech.*, *458*, 229–267.
- Teixeira, M., and S. Belcher (2010), On the structure of Langmuir turbulence, *Ocean Modell.*, *31*, 105–119.
- Thorpe, S. (2004), Langmuir circulation, *Annu. Rev. Fluid Mech.*, *36*, 55–79.
- Veron, F., and W. Melville (2001), Experiments on the stability and transition of wind-driven water surfaces, *J. Fluid Mech.*, *446*, 25–65.
- Veron, F., W. Melville, and L. Lenain (2008), Infrared techniques for measuring ocean surface processes, *J. Atmos. Oceanic Technol.*, *25*, 307–326.
- Veron, F., W. Melville, and L. Lenain (2009), Measurements of ocean surface turbulence and wave-turbulence interactions, *J. Phys. Oceanogr.*, *39*, 2310–2323.
- Yuan, Y., L. Han, F. Qiao, Y. Yang, and M. Lu (2010), A unified linear theory of wavelike perturbations under general ocean conditions, *Dyn. Atmos. Oceans*, *51*, 55–74.